

Viscoelastic finite-difference modeling

Johan O. A. Robertsson*, Joakim O. Blanch†, and William W. Symes**

ABSTRACT

Real earth media disperse and attenuate propagating mechanical waves. This anelastic behavior can be described well by a viscoelastic model. We have developed a finite-difference simulator to model wave propagation in viscoelastic media. The finite-difference method was chosen in favor of other methods for several reasons. Finite-difference codes are more portable than, for example, pseudospectral codes. Moreover, finite-difference schemes provide a convenient environment in which to define complicated boundaries. A staggered scheme of second-order accuracy in time and fourth-order accuracy in space appears to be optimally efficient.

Because of intrinsic dispersion, no fixed grid points per wavelength rule can be given; instead, we present tables, which enable a choice of grid parameters for a given level of accuracy. Since the scheme models energy absorption, natural and efficient absorbing boundaries may be implemented merely by changing the parameters near the grid boundary. The viscoelastic scheme is only marginally more expensive than analogous elastic schemes. The efficient implementation of absorbing boundaries may therefore be a good reason for also using the viscoelastic scheme in purely elastic simulations. We illustrate our method and the importance of accurately modeling anelastic media through 2-D and 3-D examples from shallow marine environments.

INTRODUCTION

We present a conditionally stable finite-difference scheme for viscoelastic wave simulation with attractive numerical characteristics. Using this scheme it is possible to model widely varying Q in highly heterogeneous media. We will start by reviewing viscoelastic theory and summarize previous work.

Elasticity is a good model for mechanical wave propagation through the earth. No real materials, however, are perfectly elastic. Wave energy is gradually converted into heat. Attenuation of propagating waveforms is, in some cases, quite significant and could be a source of erroneous results in forward modeling, inversion, and imaging if neglected (e.g., Samec and Blangy, 1992).

In this work we chose to model materials through their mechanical analogs using components such as springs and dashpots. Such a model is called a viscoelastic model which, in the elastic limit, reduces to a single spring with a spring constant corresponding to the elastic properties of the material. The so-called standard linear solid is a simple vis-

coelastic model consisting of a spring in parallel with a spring and a dashpot in series (Pipkin, 1986). The quality factor Q characterizes the attenuation of waves in a material. Q is the number of wavelengths a wave must propagate through the material before its amplitude drops by a factor $e^{-\pi}$ (White, 1992). An array of standard linear solids in parallel may be used to approximate a specific viscoelastic model with a certain Q -versus-frequency relation. Earth materials have been shown to have a nearly constant Q over the seismic frequency range [Murphy (1982) and Spencer (1981)]. A viscoelastic model consisting of a series of standard linear solids in parallel can closely approximate a constant Q over a specified frequency range. Since attenuation and dispersion are related through a Kramers-Krönig relation (Futterman, 1962), the constant Q model also yields an equally realistic dispersion relation. Futterman (1962) derived a theoretical dispersion relation for materials with a constant Q . Wuenschel (1965) experimentally showed Plexiglas and shale to exhibit this dispersion relation.

The viscoelastic stress-strain relation gives the instantaneous stress as a causal time convolution of a stress relax-

Manuscript received by the Editor May 6, 1993; revised manuscript received January 24, 1994.

*Department of Geology and Geophysics, Rice University, P.O. Box 1892, Houston, TX 77251-1892.

†The Rice Inversion Project, Dept. of Geology and Geophysics, Rice University, P.O. Box 1892, Houston, TX 77251-1892.

**The Rice Inversion Project, Department of Computational and Applied Mathematics, Rice University, P.O. Box 1892, Houston, TX 77251-1892.

© 1994 Society of Exploration Geophysicists. All rights reserved.

Reprinted from Geophysics, 59, 1444-1456. © 1994 Society of Exploration Geophysicists

ation function with the strain rate. This memory effect can be modeled in a purely differential (as opposed to integro-differential) way by adding some so-called "memory" variables to the description of the mechanical state, which obey additional time evolution equations with zero wave speeds. Since the memory variables decay rapidly and are coupled to the stress and strain, energy is dissipated. This differential description of viscoelasticity has great advantages for numerical simulation, as it is *local* in time. Day and Minster (1984), who derived a system of first-order partial differential equations by using Padé approximations to approximate the convolution in the stress-strain relation, use this approach as well as that of Carcione (1993) and Tal-Ezer et al. (1990).

Since the differential version of viscoelastic theory yields a hyperbolic system of partial differential equations, it is natural to employ explicit finite-difference schemes in simulation algorithms. Finite-difference schemes are intrinsically dispersive (Dablain, 1986), and so as not to confuse this numerical dispersion with the physical dispersion of viscoelastic waves, previous authors have employed pseudospectral schemes (Carcione et al., 1988a, 1988b, 1988c, 1993; Tal-Ezer et al., 1990). Pseudospectral schemes yield minimal numerical dispersion but employ computationally expensive discrete Fourier transforms. Use of vendor-supplied FFT packages decreases computational expense but makes such codes less portable and/or more complex than their finite-difference analogs. Also, pseudospectral schemes can accommodate only essentially periodic boundary conditions (Canuto et al., 1987).

To address the issues of portability and boundary condition flexibility, we have examined the employment of (low order) finite-difference schemes for viscoelasticity. Throughout this paper we use the $O(m, n)$ notation to describe the accuracy of the finite-difference schemes for m th-order accuracy in time and n th-order accuracy in space. We have implemented and investigated $O(2, 2)$, $O(2, 4)$, and $O(4, 4)$ accurate schemes in 1-D. These have been thoroughly investigated through convergence tests, dispersion, and stability analyses. The discrete dispersion relation for the system was found to be the product of a well-known term responsible for wave propagation and another term responsible for attenuation. The stability criteria for the viscoelastic schemes are approximately the same as for the analog elastic schemes. The Courant number must, however, be adjusted to the highest phase velocity (found at the infinite frequency) in the viscoelastic medium. We have performed convergence tests where we compared the analytic solution for single wavenumbers to the numerical solution for identical initial conditions. Based on these investigations we have also implemented 2-D and 3-D $O(2, 4)$ schemes.

In this paper, we will start with a brief review of viscoelastic theory. We will then pursue the theory by deriving the equations governing viscoelastic wave propagation and also formulate these as a system of linear first-order partial differential equations. Next we will summarize the tests we performed and present stability and dispersion analyses for the different schemes. For practical reasons we have limited this analysis to 1-D. Convergence tests of our schemes were presented in Blanch et al. (1993a, 1993b). Finally we show simulations of waves in 1-D, 2-D, and 3-D viscoelastic

media. We also demonstrate the difference between elastic and viscoelastic wave propagation in an anelastic model.

THEORETICAL MODEL—LINEAR VISCOELASTICITY

In this section, we describe a theoretical anelastic model based on viscoelastic theory, a phenomenological way to describe combined elastic and viscous behavior of materials. The basic hypothesis is that the current value of the stress tensor depends upon the history of the strain tensor. The viscoelastic hypothesis can be described as

$$\sigma_{ij} = G_{ijkl} * \dot{\epsilon}_{kl} = \dot{G}_{ijkl} * \epsilon_{kl}, \quad (1)$$

(Christensen, 1982) where $*$ denotes time convolution. The convolution transforms each strain history, $\epsilon_{ij}(t)$, into a corresponding stress history, $\sigma_{ij}(t)$. G is a fourth-order tensor-valued function of time called the relaxation function. In general, stress, strain and the relaxation function depend on both time and position. The dot denotes derivation with respect to time. The fourth-order tensor G collapses into two independent functions for an isotropic and homogeneous material. For 1-D or the special case of simple shear in an isotropic homogeneous material, equation (1) reduces to

$$\sigma = G * \dot{\epsilon} = \dot{G} * \epsilon. \quad (2)$$

The relaxation function G determines the behavior of a material. We will consider relaxation functions composed of the quite general form (Blanch et al., 1993a),

$$G(t) = M_R \left(1 - \sum_{\ell=1}^L \left(1 - \frac{\tau_{\epsilon\ell}}{\tau_{\sigma\ell}} \right) e^{-t/\tau_{\sigma\ell}} \right) \theta(t), \quad (3)$$

where M_R is the relaxation modulus of the medium (Pipkin, 1986) and $\theta(t)$ is the Heaviside function. The relaxation function in equation (3) is equivalent to a series of L standard linear solids connected in parallel (Blanch et al., 1993a), and is also the best Padé approximation of a constant Q (Day and Minster, 1984). Elements $\tau_{\epsilon\ell}$ and $\tau_{\sigma\ell}$ are the stress and strain relaxation times of the ℓ th mechanism.

Experiments have shown that earth materials generally have constant Q for both pressure and shear waves over a limited range of frequencies (e.g., Murphy, 1982; Spencer, 1981). A viscoelastic constant Q model will in turn yield a realistic dispersion relation (Futterman, 1962). To approximate a constant Q over a limited frequency band with the relaxation function in equation (3), the $\tau_{\sigma\ell}$ should be distributed logarithmically (about one per octave) as is described by Blanch et al. (1993a). The magnitude of Q is essentially determined by the difference $(\tau_{\epsilon\ell} - \tau_{\sigma\ell})$ (Blanch et al., 1993a; Liu et al., 1976). A constant (frequency independent) Q can be closely approximated by this method (Blanch et al., 1993a; Day and Minster, 1984).

VISCOELASTIC WAVE PROPAGATION

The equations describing wave propagation in viscoelastic media can be derived in terms of the creep compliance or the stress relaxation function. Here we choose to derive it from the latter. For simplicity, we will derive the equations for the 1-D case where the viscoelastic equations are the same as the viscoacoustic. From the definitions of pressure and dilatation (Gurtin, 1981) we know that,

$$\sigma = -p, \quad (4)$$

and

$$\dot{\epsilon} = v_x, \quad (5)$$

where v is the particle velocity. Taking the time derivative of equation (2) and using equations (4) and (5) leads to

$$-\dot{p} = \dot{G} * v_x. \quad (6)$$

That is,

$$-\dot{p} = M_R \left(1 - \sum_{\ell=1}^L \left(1 - \frac{\tau_{\epsilon\ell}}{\tau_{\sigma\ell}} \right) \right) v_x + M_R \left(\sum_{\ell=1}^L \frac{1}{\tau_{\sigma\ell}} \left(1 - \frac{\tau_{\epsilon\ell}}{\tau_{\sigma\ell}} \right) e^{-t/\tau_{\sigma\ell}} \right) \theta(t) * v_x. \quad (7)$$

The convolution terms in equation (7) may be eliminated by introducing so-called memory variables, which will be denoted r_ℓ (Carcione et al., 1988a). Equation (7) thereby reduces to

$$-\dot{p} = M_R \left(1 - \sum_{\ell=1}^L \left(1 - \frac{\tau_{\epsilon\ell}}{\tau_{\sigma\ell}} \right) \right) v_x + \sum_{\ell=1}^L r_\ell, \quad (8)$$

where

$$r_\ell = M_R \left(\frac{1}{\tau_{\sigma\ell}} \left(1 - \frac{\tau_{\epsilon\ell}}{\tau_{\sigma\ell}} \right) e^{-t/\tau_{\sigma\ell}} \right) \theta(t) * v_x, \quad 1 \leq \ell \leq L. \quad (9)$$

From equation (9) we see that r_ℓ are governed by convolutions of v_x with exponential functions, i.e., the kernels of r_ℓ are of exponential character. A set of first-order linear differential equations may therefore be obtained instead of the convolutions as follows. First, by taking the time derivative of equation (9), we obtain

$$\begin{aligned} \dot{r}_\ell = & -\frac{1}{\tau_{\sigma\ell}} M_R \left(\frac{1}{\tau_{\sigma\ell}} \left(1 - \frac{\tau_{\epsilon\ell}}{\tau_{\sigma\ell}} \right) e^{-t/\tau_{\sigma\ell}} \right) \theta(t) * v_x \\ & + M_R \left(\frac{1}{\tau_{\sigma\ell}} \left(1 - \frac{\tau_{\epsilon\ell}}{\tau_{\sigma\ell}} \right) e^{-t/\tau_{\sigma\ell}} \right) \delta(t) * v_x, \end{aligned} \quad 1 \leq \ell \leq L. \quad (10)$$

From equation (9) we notice that equation (10) reduces to

$$\dot{r}_\ell = -\frac{1}{\tau_{\sigma\ell}} r_\ell + M_R \frac{1}{\tau_{\sigma\ell}} \left(1 - \frac{\tau_{\epsilon\ell}}{\tau_{\sigma\ell}} \right) v_x, \quad 1 \leq \ell \leq L. \quad (11)$$

We have now derived a set of first-order linear differential equations for the memory variables. Newton's second law completes the full description of wave propagation in a viscoelastic medium. This is,

$$\rho \dot{v} = -p_x, \quad (12)$$

where ρ is the density.

Equations (8), (11), and (12) comprise the system of first-order linear differential equations of 1-D viscoelastic wave propagation in a medium with L sets of standard linear solids.

IMPLEMENTATION

We used equations (8), (11), and (12) to derive various finite-difference schemes. Dablain (1986) and Levander (1988) have shown that staggered higher-order schemes are superior to low-order schemes for modeling the elastic wave equation. A drastic improvement in simulating wave propagation is achieved when the accuracy for the spatial derivatives is increased from second to fourth order. Carcione et al. (1988a) have also stressed the importance of highly accurate modeling methods for viscoelastic wave propagation. We implemented schemes that were second-order accurate in both time and space, second-order accurate in time and fourth-order accurate in space, and fourth-order accurate in both time and space. These schemes will be referred to as the $O(2, 2)$, $O(2, 4)$, and $O(4, 4)$ schemes. The $O(4, 4)$ scheme was a so-called compact scheme (Dablain, 1986), which increases accuracy in time without expanding the finite-difference stencil. We found the $O(2, 4)$ scheme to be superior to the $O(2, 2)$ and $O(4, 4)$ schemes (Blanch et al., 1993a). The $O(2, 4)$ scheme has considerably better dispersion properties than the $O(2, 2)$ and requires approximately only 50 percent more calculations per space-time grid point. As Blanch et al. (1993a) point out, the more accurate $O(4, 4)$ scheme is unreasonably more expensive than the $O(2, 4)$ scheme, particularly for higher dimensions. The following analysis is therefore only concerned with the $O(2, 4)$ scheme unless otherwise stated.

To approximate the time derivatives, we used the leap-frog scheme (Kreiss and Oliger, 1973) for equations (8) and (12). We chose to use a stiff solver for equation (11), since these equations may become stiff when some $\tau_{\sigma\ell}$ are small compared to Δt (time step), as may be the case when employing several relaxation mechanisms (Table 3). A stiff solver therefore ensures a stable scheme for arbitrarily accurate modeling of Q . The Crank-Nicolson scheme (Kreiss and Oliger, 1973) proved to be adequate, and since equation (11) consists of simple first-order *ordinary differential equations* with source terms, the usually implicit Crank-Nicolson scheme has an explicit implementation, which is only marginally more expensive than a conventional explicit scheme. A fruitful realization of an $O(2, 4)$ scheme with the above specifications for one relaxation mechanism is the *staggered* scheme defined in equations (13) through (15):

$$\begin{aligned} & \frac{p_j^{n+1/2} - p_j^{n-1/2}}{\Delta t} \\ & = -M_R \frac{\tau_{\epsilon\ell}}{\tau_{\sigma\ell}} \frac{-v_{j+3/2}^n + 27v_{j+1/2}^n - 27v_{j-1/2}^n + v_{j-3/2}^n}{24\Delta x} \\ & \quad - \frac{1}{2} (r_j^{n+1/2} + r_j^{n-1/2}), \end{aligned} \quad (13)$$

$$\begin{aligned} & \frac{r_j^{n+1/2} - r_j^{n-1/2}}{\Delta t} \\ & = -\frac{1}{2\tau_{\sigma\ell}} (r_j^{n+1/2} + r_j^{n-1/2}) - M_R \frac{1}{\tau_{\sigma\ell}} \times \left(\frac{\tau_{\epsilon\ell}}{\tau_{\sigma\ell}} - 1 \right) \end{aligned}$$

$$\times \left(\frac{-v_{j+3/2}^n + 27v_{j+1/2}^n - 27v_{j-1/2}^n + v_{j-3/2}^n}{24\Delta x} \right), \quad (14)$$

$$\rho \frac{v_j^{n+1/2} - v_j^{n-1/2}}{\Delta t} = - \frac{-p_{j+3/2}^n + 27p_{j+1/2}^n - 27p_{j-1/2}^n + p_{j-3/2}^n}{24\Delta x}, \quad (15)$$

where Δt is the time step and Δx is the spatial step. Indices n and j correspond to time and space coordinates respectively [$p_j^n = p(n\Delta t, j\Delta x)$]. The scheme in equations (13) through (15) can be implemented such that it is necessary to store only one time level of each field by first updating the pressure field partially, then updating the memory variable field, and finally updating the pressure field completely.

STABILITY ANALYSIS

The discussion in this and the following section is restricted to one memory variable, $L = 1$. We used von Neumann analysis as well as numerical experiments to investigate the stability of different finite-difference schemes. Our study of the von Neumann condition was numerical; we computed the eigenvalues of the amplification matrix on a fine grid in the wavenumber space. Some realizations were found to be conditionally stable whereas others were intrinsically unstable, even though the same schemes, leap-frog and Crank-Nicolson, were used to update the system of equations. Small changes in equation (14) are sufficient to produce either conditionally stable or unstable schemes. The two possible *staggered* formulations are both conditionally stable, thus the staggered scheme in equations (13) through (15) is conditionally stable. A more complete discussion of the different schemes may be found in Blanch et al. (1993c, 1993d).

The stability criteria for the conditionally stable schemes are similar to analog elastic schemes (Dablain, 1986; Levander, 1988). The Courant number ($c\Delta t/\Delta x$, where c is the velocity) for viscoelastic schemes has to be adjusted to the highest phase velocity, which is found at infinite frequency, $c_{\max} = \sqrt{\tau_e M_R/\tau_\sigma \rho}$.

DISPERSION ANALYSIS

Viscoelastic media are intrinsically dispersive. The phase velocity increases with frequency as shown by Futterman (1962) and Wuenschel (1965). This is evident in Figure 1. In addition, finite-difference methods for wave propagation introduce numerical dispersion because of the time and space discretization. Hence, we are studying dispersive media with dispersive methods. We must therefore ensure that the influence of numerical dispersion is minimal.

The discrete finite-difference schemes are Fourier transformed to the frequency-wavenumber domain where they are compared to the analytical dispersion of the viscoelastic medium. The numerical dispersion originates from two places in our schemes. First, unwanted dispersion might be introduced in the equation governing the memory variable r . A more familiar type of numerical dispersion is introduced

through the part of the scheme governing the wave propagation. The dispersion relation for the viscoelastic schemes must be solved numerically, most conveniently through an iterative method.

Because of the dependence on Q and the complicated analytical dispersion relations, it is not possible to derive a simple rule of thumb for the number of grid points per wavelength needed to ensure sufficiently small numerical dispersion. Instead we performed a thorough study where we calculated the relative error for the numerically modeled velocity for different values of Q , $\eta = \Delta t/\tau_\sigma$, and Courant numbers. The Courant number was varied from a fifth of the stability limit to the stability limit. The results are presented in Tables 1 and 2, where the necessary number of grid points per wavelength to ensure less than 5 percent or 2 percent dispersion error are listed.

The dispersion relations for the $O(2, 2)$ and $O(2, 4)$ schemes may be written as a factor for the numerical dispersion originating from an elastic scheme multiplied with a factor for the numerical dispersion from the equation for

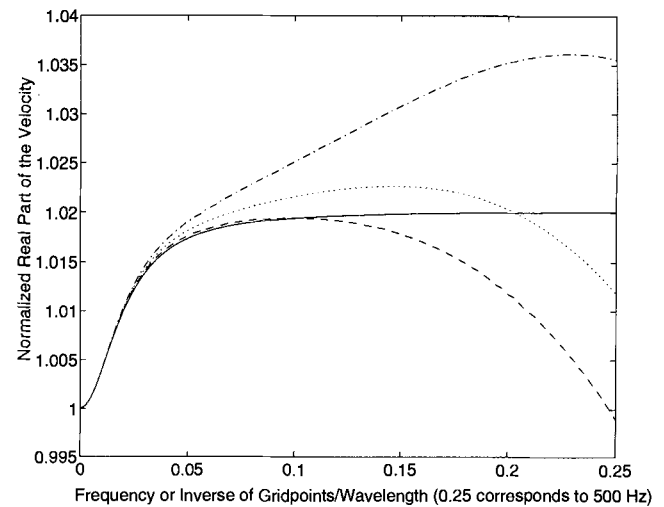


FIG. 1. Dispersion curves (the normalized real part of the velocity versus the inverse of grid points per wavelength). The maximum value on the x-axis corresponds to a frequency of 500 Hz. This frequency has to be given since the viscoelastic medium is intrinsically dispersive. Maximum attenuation is found at 40 Hz. The Courant number has the values 0.2, 0.4, and 0.6. Solid: True dispersion. Dashed: Courant number = 0.2. Dotted: Courant number = 0.4. Dash dotted: Courant number = 0.6.

Table 1. Number of grid points per wavelength necessary to obtain less than 5 percent dispersion error, with a Courant number ranging from the stability limit to a fifth of the stability limit, ($\eta = \Delta t/\tau_\sigma$).

5 percent error	$\eta = 0.1$	$\eta = 0.7$	$\eta = 1.3$	$\eta = 1.9$
$Q = 10$	4	5	5	4
$Q = 50$	5	5	5	5
$Q = 200$	5	5	5	5
$Q = 1000$	5	5	5	5
$Q = 10000$	5	5	5	5

the memory variable. The viscoelastic dispersion curves demonstrate the same characteristics as their elastic analogs (Dablain, 1986; Levander, 1988). Dispersion curves for the $O(2, 4)$ scheme [equations (13) through (15)] are plotted in Figure 1. Since viscoelastic media attenuate propagating wave energy, it is necessary to confirm that the finite-difference scheme models the damping of the waves properly. The scheme models the damping very accurately for a wide range of Courant numbers, as can be seen in Figure 2 where damping curves, corresponding to the dispersion curves in Figure 1, are plotted. The dispersion relation for the scheme is

$$\sin^2(\omega_0/2) = \lambda^2 \sin^2(k_0/2) \left(\frac{13 - \cos(k_0)}{12} \right)^2 \times (1 + F(\omega_0, \Delta t, \tau_e, \tau_\sigma)), \quad (16)$$

where

$$F = \tau(1 + \eta G),$$

$$G = \frac{\cos(\omega_0/2)}{i \sin(\omega_0/2) - \eta \cos(\omega_0/2)},$$

$$\lambda = c\Delta t/\Delta x, \quad \omega_0 = \omega\Delta t, \quad k_0 = k\Delta x, \quad \eta = \Delta t/\tau_\sigma,$$

$$\tau = \tau_e/\tau_\sigma - 1, \quad i = \sqrt{-1},$$

c is the velocity, ω is the angular frequency, and k is the wavenumber. If the term $F(\omega_0, \Delta t) \equiv 0$ (which implies that $\tau_e = \tau_\sigma$), the dispersion relation collapses to its corresponding elastic analog.

In addition to the dispersion analysis, we have also performed convergence tests on the $O(2, 2)$, $O(2, 4)$, and $O(4, 4)$ schemes and found them to converge towards the exact solution according to the prescribed accuracy (Blanch et al., 1993b).

NUMERICAL 1-D EXAMPLE

We performed several simulations for different schemes using a Ricker wavelet with a central frequency of 35 Hz propagating in the positive x direction in a 2000-m long homogeneous interval with periodic boundary conditions. One of these experiments is described below.

Table 2. Number of grid points per wavelength necessary to obtain less than 2 percent dispersion error, with a Courant number ranging from the stability limit to a fifth of the stability limit, ($\eta = \Delta t/\tau_\sigma$.)

2 percent error	$\eta = 0.1$	$\eta = 0.7$	$\eta = 1.3$	$\eta = 1.9$
$Q = 10$	7	8	7	7
$Q = 50$	8	8	8	8
$Q = 200$	8	8	8	8
$Q = 1000$	8	8	8	8
$Q = 10000$	8	8	8	8

Considerations on a practical number of relaxation mechanisms

The relaxation modulus M_R (which corresponds to the bulk modulus in the elastic case), was 8 GPa and the density 2000 kg/m³. This leads to a velocity of 2000 m/s in the 0 Hz limit. In Table 3 we display three pairs of relaxation mechanisms, obtained through the optimization algorithm described by Blanch et al. (1993a) and briefly above, which yield an essentially constant Q of 200 between 20 and 80 Hz. In Figure 3 we compare a snapshot at 2.25 s and a Q of 200 using the $O(2, 4)$ scheme for one pair of relaxation mechanisms ($\tau_e = 4.2654$ ms, $\tau_\sigma = 4.2230$ ms) to an identical simulation, but for a case where we used three pairs of relaxation mechanisms (Table 3). The difference is small indicating that the optimization of a constant Q may not be as crucial as might have been anticipated in simulating viscoelastic wave propagation. For practical purposes, it might even be sufficient to use even fewer pairs of relaxation mechanisms than one per octave, as we stated as a good rule of thumb. The explanation for this is found from the memory variables. The magnitude of the fields corresponding to the different relaxation mechanisms varies dramatically so that the main contribution to the viscoelastic modeling stems from the memory variable corresponding to the first set of relaxation mechanisms (see Blanch et al., 1993a).

2-D AND 3-D VISCOELASTIC MODELING

The results from the 1-D case described above are easily generalized to higher dimensions (see Appendix). Our im-

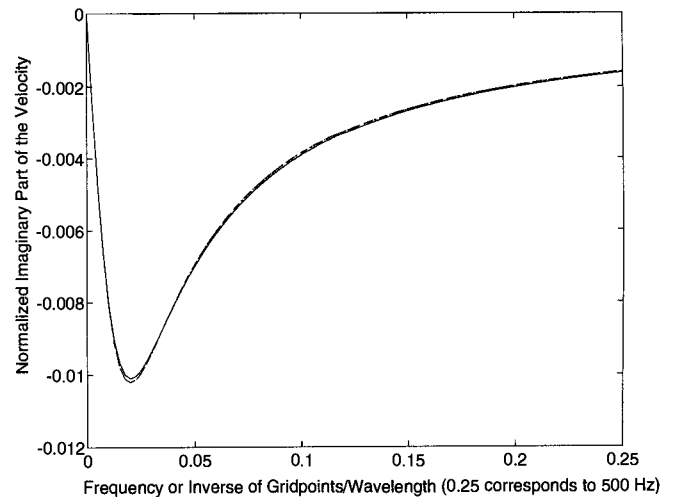


FIG. 2. Damping curves (the normalized imaginary part of the velocity versus the inverse of grid points per wavelength). The maximum value on the x-axis corresponds to a frequency of 500 Hz. This frequency has to be given since the viscoelastic medium is intrinsically dispersive. Maximum attenuation is found at 40 Hz. Notice that there are four curves plotted in the figure. These do, however, fall extremely close to each other (only two curves are barely distinguishable), indicating how well our scheme models the true attenuation at different Courant numbers. The Courant number has the values 0.2, 0.4, and 0.6. Solid: True dispersion. Dashed: Courant number = 0.2. Dotted: Courant number = 0.4. Dash dotted: Courant number = 0.6.

plementation of the 2-D viscoelastic equations requires 14 fields of variables to be stored simultaneously and 120 calculations per grid point and time step. The 3-D implementation requires 21 fields of variables to be stored simultaneously and 220 calculations per grid point and time step. The analog elastic schemes require 8 fields and 70 calculations per grid point in 2-D, and 12 fields and 160 calculations per grid point in 3-D. In the 2-D viscoelastic case of 1 relaxation mechanism, both for the *P*-waves and the *SV*-waves, the analogs of equations (8), (11), and (12) are,

$$\left\{ \begin{aligned} \frac{\partial \sigma_{xy}}{\partial t} &= \mu \frac{\tau_e^s}{\tau_\sigma} \left(\frac{\partial v_x}{\partial y} + \frac{\partial v_y}{\partial x} \right) + r_{xy} \\ \frac{\partial \sigma_{xx}}{\partial t} &= \pi \frac{\tau_e^p}{\tau_\sigma} \left(\frac{\partial v_x}{\partial x} + \frac{\partial v_y}{\partial y} \right) - 2\mu \frac{\tau_e^s}{\tau_\sigma} \frac{\partial v_y}{\partial y} + r_{xx} \\ \frac{\partial \sigma_{yy}}{\partial t} &= \pi \frac{\tau_e^p}{\tau_\sigma} \left(\frac{\partial v_x}{\partial x} + \frac{\partial v_y}{\partial y} \right) - 2\mu \frac{\tau_e^s}{\tau_\sigma} \frac{\partial v_x}{\partial x} + r_{yy} \\ \frac{\partial v_x}{\partial t} &= \frac{1}{\rho} \left(\frac{\partial \sigma_{xx}}{\partial x} + \frac{\partial \sigma_{xy}}{\partial y} \right) \\ \frac{\partial v_y}{\partial t} &= \frac{1}{\rho} \left(\frac{\partial \sigma_{xy}}{\partial x} + \frac{\partial \sigma_{yy}}{\partial y} \right) \\ \frac{\partial r_{xy}}{\partial t} &= -\frac{1}{\tau_\sigma} \left(r_{xy} + \mu \left(\frac{\tau_e^s}{\tau_\sigma} - 1 \right) \left(\frac{\partial v_x}{\partial y} + \frac{\partial v_y}{\partial x} \right) \right) \\ \frac{\partial r_{xx}}{\partial t} &= -\frac{1}{\tau_\sigma} \left(r_{xx} + \pi \left(\frac{\tau_e^p}{\tau_\sigma} - 1 \right) \left(\frac{\partial v_x}{\partial x} + \frac{\partial v_y}{\partial y} \right) \right. \\ &\quad \left. - 2\mu \left(\frac{\tau_e^s}{\tau_\sigma} - 1 \right) \frac{\partial v_y}{\partial y} \right) \\ \frac{\partial r_{yy}}{\partial t} &= -\frac{1}{\tau_\sigma} \left(r_{yy} + \pi \left(\frac{\tau_e^p}{\tau_\sigma} - 1 \right) \left(\frac{\partial v_x}{\partial x} + \frac{\partial v_y}{\partial y} \right) \right. \\ &\quad \left. - 2\mu \left(\frac{\tau_e^s}{\tau_\sigma} - 1 \right) \frac{\partial v_x}{\partial x} \right), \end{aligned} \right. \quad (17)$$

where

σ_{ij} denotes the ij th component of the symmetric stress tensor.

v_i denotes the i th component of the velocity.

r_{ij} are the memory-variables. Three are needed for the simplest 2-D case with one relaxation mechanism each for the *P*-waves and the *SV*-waves (see Appendix).

τ_e^p and τ_e^s are the strain relaxation times for the *P*- and *SV*-waves, respectively.

τ_σ is the stress relaxation time both for the *P*- and *SV*-waves. It is possible to use the same stress relaxation time both for the *P*- and *SV*-waves (Blanch et al., 1993d).

μ is the relaxation modulus corresponding to *SV*-waves and is the analog of the Lamé constant μ in the elastic case.

π is the relaxation modulus corresponding to *P*-waves analogous to $\lambda + 2\mu$ in the elastic case, where λ and μ are the Lamé constants.

We have defined the relaxation functions so that these correspond to *P*- and *SV*-waves, respectively. We are therefore able to derive the relaxation mechanisms directly from constraints on the quality factors for the *P*- and *SV*-waves separately, analogous to what was done in the 1-D case described above. This is why a relaxation modulus π , not corresponding to a single Lamé constant, is introduced. The derivation of equation (17) can be found in the Appendix.

Stability and accuracy issues are treated as was described above. The scheme has the same properties as the 1-D $O(2, 4)$ scheme. Leap-frog in time and fourth-order-centered differences in space are used for the equations governing velocity and stress components. Crank-Nicolson in time and fourth-order-centered differences in space are used for the equations governing the memory variables. The dispersion relation for the 2-D viscoelastic scheme has two solutions, one corresponding to the *P*-wave velocity and one corresponding to the *S*-wave velocity. This yields simple modeling of fluid-solid boundaries since there is no coupling between *P*-waves and *S*-waves in a homogeneous medium.

We believe that our viscoelastic code has applications in modeling many realistic situations. To demonstrate this, we will next show two examples from shallow marine environ-

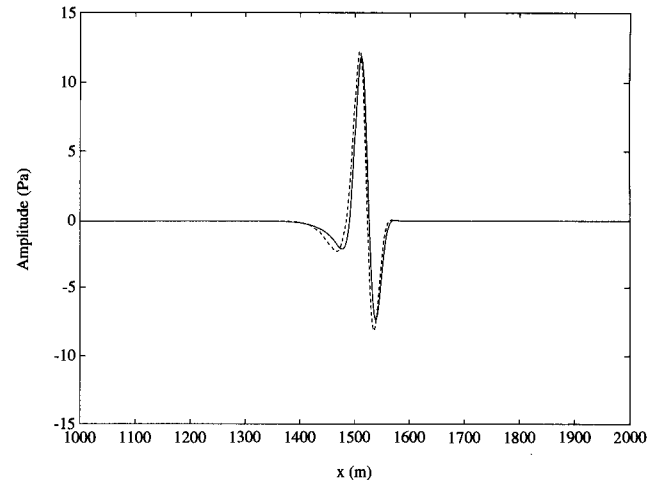


FIG. 3. Snapshots at 2.25 s comparing experiments with a constant Q of 200 and three relaxation mechanisms (listed in Table 3) to one with one relaxation mechanism using the $O(2, 4)$ scheme at a Courant number of 0.2 and a spatial step size of 2 m. Solid: Three pairs of relaxation mechanisms. Dashed: One pair of relaxation mechanisms.

Table 3. Optimized relaxation mechanisms to yield a constant Q of 200 between 20 and 80 Hz.

Pair	τ_e (ms)	τ_σ (ms)
1	8.0186	7.9578
2	1.1565	1.1488
3	0.51773	0.51705

ments where neglecting anelastic effects seriously limits realistic analyses.

Common features on the continental shelf along the U.S. Gulf coast include incised valleys, created by a variety of fluvial systems (ancient rivers and deltas, etc.), and oxbow lakes originating from ancient meandering rivers (Siringan, 1993). During retrogradation such systems are back-filled with clastic sediments. These sediment fills are highly anelastic and, moreover, their properties change with time as they are compressed by younger deposits.

Sedimentologists mapping shallow sediment structures on the continental shelf commonly use sources (e.g., water guns and unibombs) with significantly higher frequency content than sources used in conventional seismic exploration. In both examples, we used Ricker wavelet sources with center-frequencies of 80 Hz in the 2-D example and 120 Hz in the 3-D example. The Ricker wavelet is spherically symmetric and was inserted as a pressure pulse in the water column, constant in the first two time steps. We chose to model only one set of relaxation mechanisms and thereby obtained a quasi-constant Q approximation that serves our purposes well.

We chose not to model the water surface since multiple reflections from this interface would complicate a simple analysis of the wavefield. Instead we used absorbing boundaries all around the grid by increasing the attenuation towards the edges to a Q of 2 for both P - and S -waves, which in effect is a sponge filter (Israeli and Orzag, 1981). Because of the intrinsic viscoelastic dispersion, we also tuned the Lamé constants in the absorbing region to minimize impedance reflections. The method enables us to use very thin absorbing boundaries (20 grid points or approximately 2 wavelengths thick in the 3-D example).

Numerical example 1—2-D wave propagation in a sediment feature on the continental shelf (e.g., an incised valley)

In this example, we modeled a seismic experiment using an 80 Hz Ricker wavelet and a typical cross-section of an incised valley (Siringan, 1993). This is illustrated in Figure 4 and the material properties are listed in Table 4. The model is 190 m in the vertical direction, of which the upper 70 m are water (see Figure 4), and 640 m in the horizontal direction. We have cut out the absorbing frame in the energy snapshots in Figures 5a through d and Figures 6a through d. A 1 m grid spacing was used in both spatial directions and the time step was 0.15 ms, which leads to a maximum Courant number of 0.33, which is well below the stability limit for our scheme.

In Figures 5a through d, we show P - and SV -wave energy snapshots of a viscoelastic simulation using the material properties in Table 4. In Figures 6a through d we show snapshots from the analog experiment in the elastic limit where we have set all Q values in Table 4 to 10 000. The SV -wave energy snapshots have been amplified three times in comparison to the P -wave energy snapshots. In Figures 5a and b, and 6a and b, we show the P - and SV -wave energy snapshots at 0.05 s for the viscoelastic and the elastic simulation, respectively. In the snapshots for the P -wave energy, reflections from the different sediment layers are clearly visible. There is a strong conversion of P -waves to SV -waves at the different boundaries. SV -waves are gener-

ated where the P -wave intersects the boundaries of the model. This gives the impression that the SV -waves are following the boundaries between the different sediment layers. This effect is not as prominent at the water-solid boundary. There is hardly any difference between the elastic and viscoelastic case. The energy from the waves is also well absorbed by the boundaries (no reflections are visible). In Figures 5c and d, and 6c and d, we show the P - and SV -wave energy snapshots at 0.2 s. The amplitude of the P -headwave is significantly reduced from propagating through the viscoelastic sediments. The SV -waves in the viscoelastic medium clearly have smaller amplitudes compared to the SV -waves in the elastic medium. Details are also more difficult to observe in the snapshot from the viscoelastic simulation since the wave energy is attenuated and dispersed. Moreover, conversions from SV - to P -waves at the layer boundaries induce P -wave energy in the water column. This

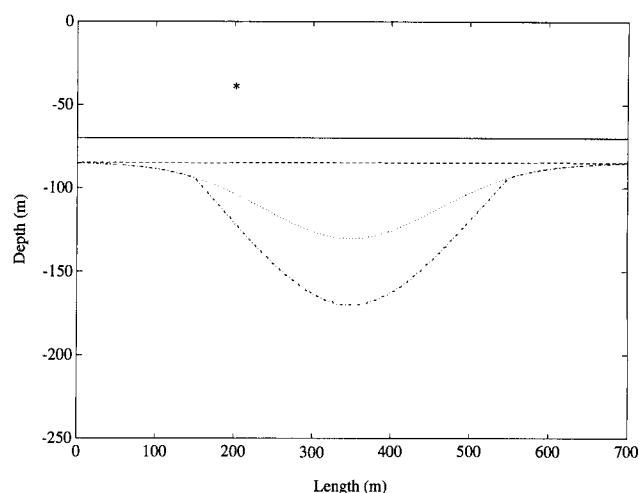


FIG. 4. The model used in the incised valley experiment. The area above the solid line is water. The area between the solid and the dashed line represents Holocene transgressive marine deposits. The area between the dashed and the dotted line represents transgressive marine overlying transgressive estuarine deposits. The area between the dotted and the dash-dotted line represents regressive fluvial deposits. The dotted line indicates the bay line, the boundary between the regressive and transgressive sequences. The area below the solid line and above the dash-dotted line are late Pleistocene to Holocene deposits. The area below the dash-dotted line represents early Wisconsinian regressive deposits. The star shows the position of the source.

Table 4. The average material properties used for the incised valley model, where v_p is the velocity of P -waves and Q_p its quality factor, v_s is the S -wave velocity and Q_s its quality factor, and ρ is the density. Layers 1, 2, 3, and 4 denote the different sediment layers.

	Water	Layer 1	Layer 2	Layer 3	Layer 4
v_p (km/s)	1.52	1.60	1.75	1.9	2.2
Q_p	10 000	40	50	50	100
v_s (km/s)	0	0.4	0.8	1.0	1.2
Q_s	0	30	35	45	70
ρ (g/cm ³)	1.05	1.3	1.5	1.5	2.0

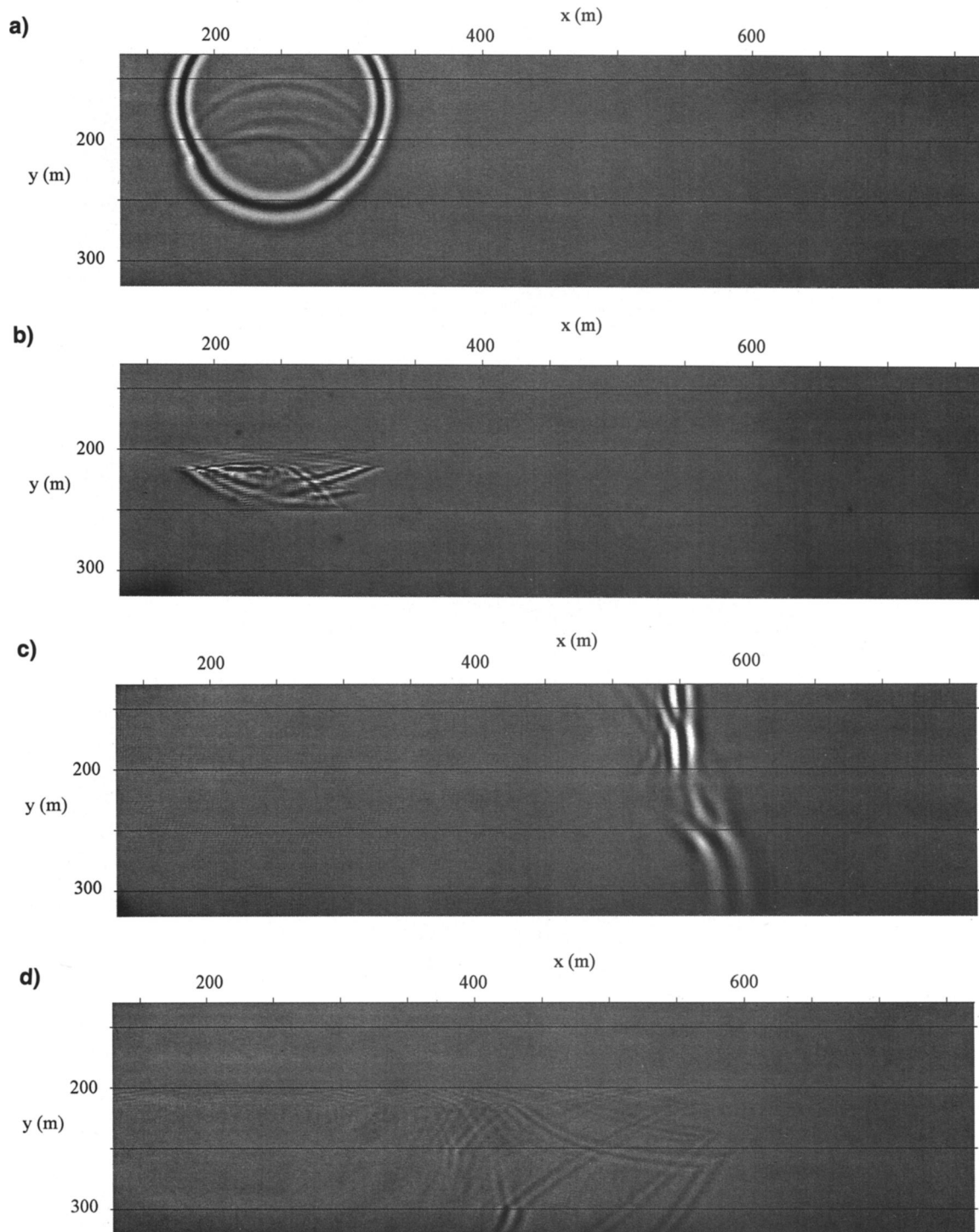


FIG. 5. Snapshots of *P*-wave energy (a) and (c) and *SV*-wave energy (b) and (d) for the viscoelastic incised valley model. The material properties are listed in Table 4. The absorbing boundaries are cut out from the snapshots. The unit of the scales on the axes are meters and are relative to the upper left corner in the grid when the absorbing boundaries are included. (a) *P*-wave energy for the viscoelastic model at 0.05 s. (b) *SV*-wave energy for the viscoelastic model at 0.05 s. (c) *P*-wave energy for the viscoelastic model at 0.2 s. (d) *SV*-wave energy for the viscoelastic model at 0.2 s.

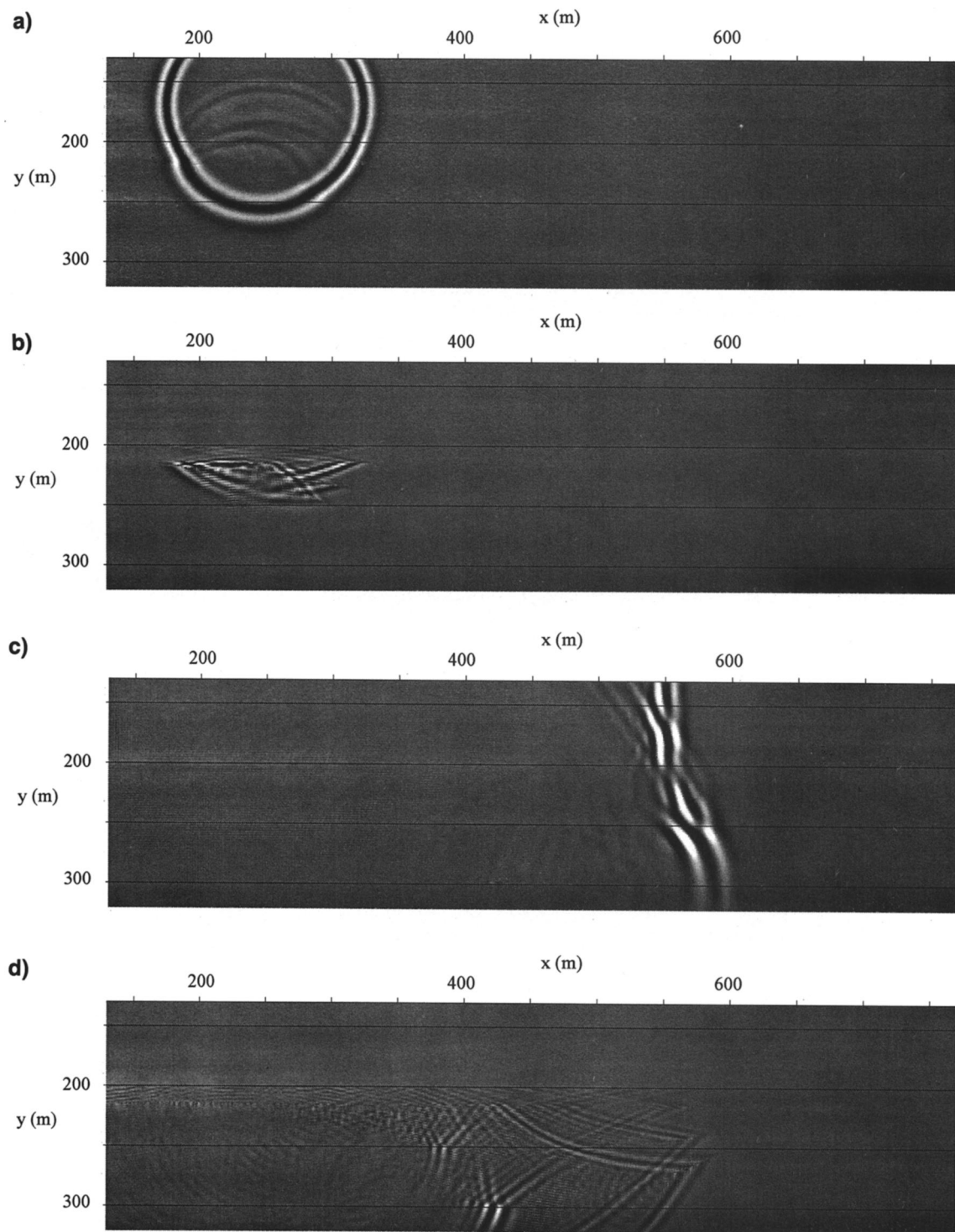


FIG. 6. Snapshots of P -wave energy (a) and (c) and SV -wave energy (b) and (d) for the elastic incised valley model. The material properties are listed in Table 4. The absorbing boundaries are cut out from the snapshots. The unit of the scales on the axes are meters and are relative to the upper left corner in the grid when the absorbing boundaries are included. (a) P -wave energy for the elastic model at 0.05 s. (b) SV -wave energy for the elastic model at 0.05 s. (c) P -wave energy for the elastic model at 0.2 s. (d) SV -wave energy for the elastic model at 0.2 s.

process is much weaker in the viscoelastic case compared to the elastic case.

Numerical example 2—3-D wave propagation in a sediment feature on the continental shelf (e.g., an oxbow lake)

In this example we chose a Ricker wavelet with a center frequency of 120 Hz to investigate a shallow subbottom sediment feature of 3-D character, modeled after an oxbow lake (Siringan, 1993). The grid-spacing was 1 m in all spatial directions. The grid-size was $200 \times 100 \times 100$ m, including

Table 5. The average material properties used for the oxbow lake model, where v_p is the velocity of P -waves and Q_p its quality factor, v_s is the S -wave velocity and Q_s its quality factor, ρ is the density. Layers 1, 2, and 3 denote the different sediment layers.

	Water	Layer 1	Layer 2	Layer 3
v_p (km/s)	1.52	1.60	1.9	2.2
Q_p	10 000	40	50	100
v_s (km/s)	0	0.4	1.0	1.2
Q_s	0	30	45	70
ρ (g/cm ³)	1.05	1.3	1.5	2.0

the absorbing boundaries. The simulation was performed at 75 percent of the stability limit and took 55 minutes on an IBM RS 6000/580. In Table 5 we display the material properties used in this experiment. The upper 50 m are occupied by a water column in which the source is located. Below this a 4-m thick homogeneous flat marine sediment layer is present. This overlays the oxbow lake structure illustrated in Figure 7a. The sediments below the oxbow lake are early Wisconsinian regressive deposits. In Figures 7b and 7c, we display perpendicular vertical cross-sections through the grid.

In Figures 8a and c, we display P -wave energy snapshots at 25 ms. Figure 8a is taken along the center of the longest (200 m) dimension in the vertical plane. We see clearly that the absorbing boundaries efficiently absorb incoming energy at the top of the model. Reflections from the bottom of the back-filled oxbow lake are also visible. The snapshot in Figure 8c is perpendicular to the snapshot in Figure 8a, through the center of the grid and in the vertical plane. In Figures 8b and 8d, we display S -wave energy snapshots after 50 ms from the same planes as the snapshots in Figures 8a and 8c. The 3-D effects are more pronounced here. In Figure 8b, we can see how S -wave energy gets trapped in the uppermost marine sediment layer. The S -waves are damped

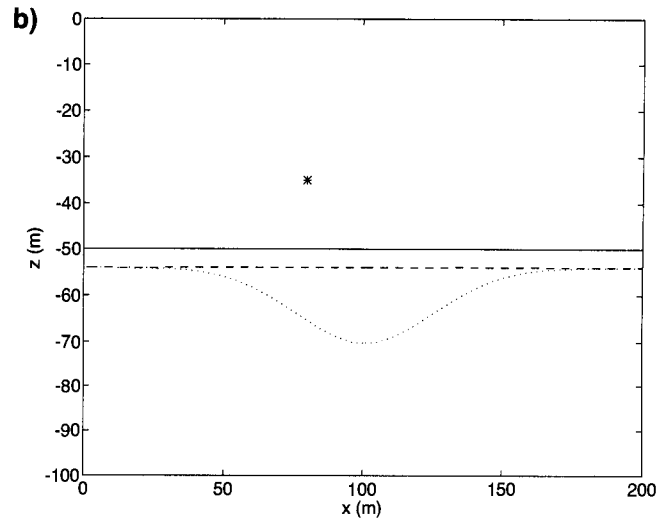
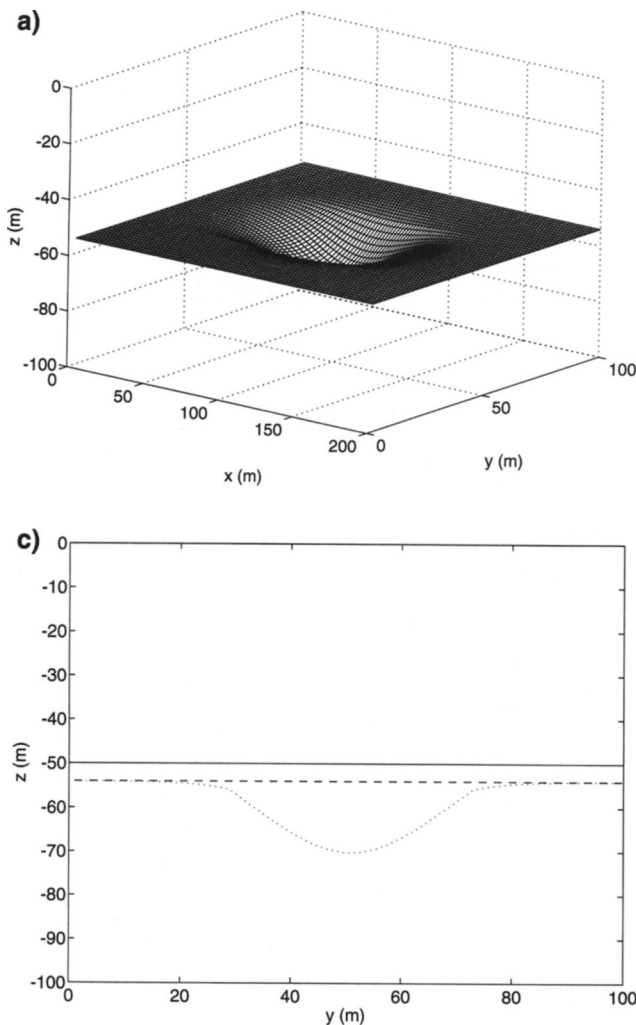


FIG. 7. The model used in the 3-D oxbow lake experiment. (a) A 3-D view of the layer underlying the oxbow lake. (b) and (c) Vertical cross-sections through the center of the model in the xz - and yz -planes. The area above the solid line is water. The area between the solid and the dashed line represents Holocene transgressive marine deposits (Layer 1 in Table 5). The area between the dashed and the dotted line represent regressive fluvial deposits (Layer 2 in Table 5). The area below the dotted line represents early Wisconsinian regressive deposits (Layer 3 in Table 5). The star shows the position of the source.

by the sediments and the strongest feature is the direct S -wave in the lowermost layer where Q is the highest. The wave pattern is quite complicated in the region of the oxbow lake. In Figure 8d we clearly see how S -wave energy is trapped in this feature.

CONCLUSIONS

Viscoelasticity provides a powerful tool for modeling real earth media. The viscoelastic relaxation functions can easily be tuned to resemble the attenuative and dispersive effects that real earth materials have on propagating waves. We investigated several finite-difference schemes, all of which used leap-frog time and space differencing in the equations for the stress and velocity updates. To accommodate the range of relaxation times occurring in very accurate approximations of constant Q , we found it necessary to use a stiff solver for the memory variables. The Crank-Nicolson method produced a robust and sufficiently accurate scheme for the memory variables, which is nearly as computationally efficient as less robust explicit schemes. We also found it to be of utmost importance to choose the stencil for the memory variables correctly to obtain a conditionally stable scheme.

The scheme we decided to adapt and implement in two and three dimensions is staggered and second-order accurate

in time and fourth-order accurate in space. It exhibits very attractive dispersion and attenuation properties. The stability is controlled by proper choice of time and space steps and is given in terms of the Courant number. Because of a complicated dispersion relation, we provide a table as a guide for the choice of the necessary number of grid points per wavelength necessary to ensure an accurate simulation.

Through 2-D and 3-D examples, we have shown the applicability of the codes. Efficient and computationally inexpensive absorbing boundaries are easy to implement. This property may as a matter of fact be a good reason for simulating elastic wave propagation using a viscoelastic code, especially in 2.5-D and 3-D models where high incidence angle energy may be difficult to absorb otherwise.

We conclude that it is fully possible to use finite-difference methods to simulate wave propagation through dispersive and attenuative viscoelastic media. It is easy to choose simulation accuracy and the code is highly portable. We have done viscoelastic wave propagation simulations using our schemes and have achieved high performance on several different computers such as the IBM RS 6000/580, Steller Stardent 2000, various SUN workstations, the Cray YMP/8, and the hypercube i860.

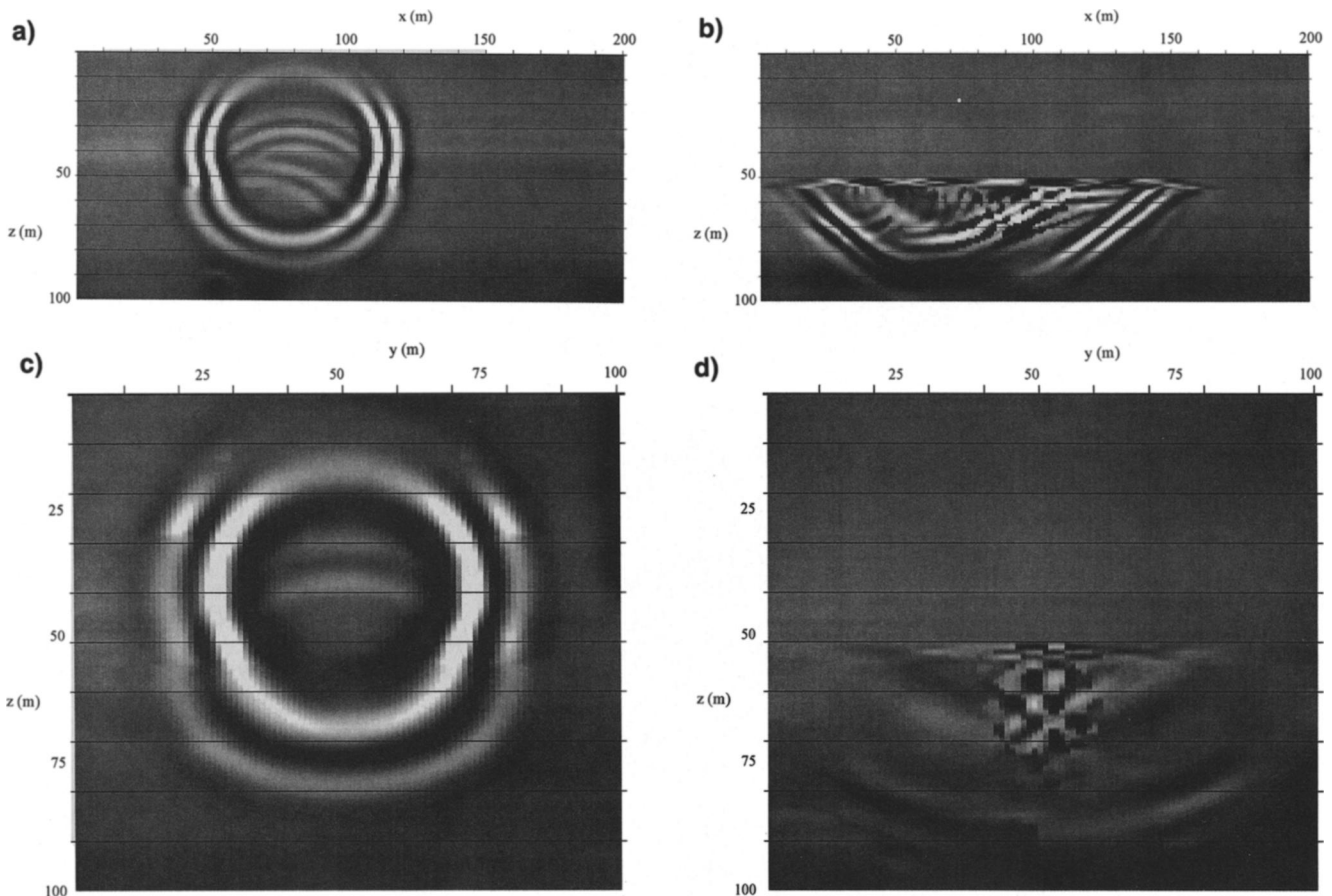


FIG. 8. Snapshots from the 3-D oxbow lake experiment. (a) and (b) illustrate energy snapshots in the xz -plane (see Figure 7b) for the P -wave field at 25 ms and the S -wave field at 50 ms. (c) and (d) illustrate energy snapshots in the yz -plane (Figure 7c) for the P -wave field at 25 ms and the S -wave field at 50 ms.

The code has primarily been developed to provide a useful tool for scattering and inversion projects. At present, we are doing 2-D and 3-D viscoelastic seafloor scattering experiments, Q -inversion studies, as well as forward modeling. The code is also a component in Hybrid Adaptive Regime Visco-Elastic Simulation Technique (HARVEST), an adaptive wave-propagation regime simulation technique developed at Rice University.

ACKNOWLEDGMENTS

This work was supported by ONR grants N00014-89-J3015 and N00014-89-J1115. We wish to express our sincere gratitude to Alan Levander of the Department of Geology and Geophysics at Rice University for support and useful input during the work. During the development of the code, we used the Cray YMP at San Diego Super Computer Center, the POPS Cray YMP at Stennis Space Center, the IBM RS 6000/580, the Steller Stardent 2000, and the hypercube i860 at Rice University. Metaplot™ graphics were provided courtesy of The Rice Inversion Project (TRIP), an industrial research consortium.

REFERENCES

- Blanch, J. O., Robertsson, J. O. A., and Symes, W. W., 1993a, Viscoelastic finite-difference modeling: Tech. Rep. 93-04, Department of Computational and Applied Mathematics, Rice University.
- 1993b, Viscoelastic finite-difference modeling, in Kleinman, R., Angell, T., Colton, D., Santosa, F., and Stakgold, I., Eds., Mathematical and numerical aspects of wave propagation: SIAM, 69–81.
- 1993c, Viscoelastic finite-difference modeling: 63rd Ann. Internat. Mtg., Soc. Expl. Geophys., Expanded Abstracts, 990–993.
- 1993d, Viscoelastic finite difference modeling II: Tech. Rep. 93-16, Department of Computational and Applied Mathematics, Rice University.
- Canuto, C., Hussaini, M. Y., Quarteroni, A., and Zang, T. A., 1987, Spectral methods in fluid dynamics: Springer-Verlag, New York, Inc.
- Carcione, J. M., 1993, Seismic modeling in viscoelastic media: Geophysics, 58, 110–120.
- Carcione, J. M., Kosloff, D., and Kosloff, R., 1988a, Wave propagation simulation in a linear viscoacoustic medium: Geophys. J. Roy. Astr. Soc., 93, 393–407.
- 1988b, Viscoacoustic wave propagation simulation in the earth: Geophysics, 53, 769–777.
- 1988c, Wave propagation simulation in a linear viscoelastic medium: Geophys. J. Roy. Astr. Soc., 95, 597–611.
- Christensen, R. M., 1982, Theory of viscoelasticity—An introduction: Academic Press, Inc.
- Dablain, M. A., 1986, The application of high-order differencing to the scalar wave equation: Geophysics, 51, 127–139.
- Day, S. M., and Minster, J. B., 1984, Numerical simulation of attenuated wavefields using a Padé approximant method: Geophys. J. R. Astr. Soc., 78, 105–118.
- Futterman, W. I., 1962, Dispersive body waves: J. Geophys. Res., 67, 5279–5291.
- Gurtin, M. E., 1981, An introduction to continuum mechanics: Academic Press, Inc.
- Israeli, M., and Orzag, S. A., 1981, Approximation of radiating boundary conditions: J. Comput. Phys., 41, 115–135.
- Kreiss, H. O., and Oliger, J., 1973, Methods for the approximate solution of time dependent problems: GARP publications series No. 10.
- Levander, A. R., 1988, Fourth-order finite-difference P -SV seismograms: Geophysics, 53, 1425–1436.
- Liu, H. P., Anderson, D. L., and Kanamori, H., 1976, Velocity dispersion due to anelasticity; implications for seismology and mantle composition: Geophys. J. Roy. Astr. Soc., 47, 41–58.
- Murphy, W. F. III, 1982, Effects of partial saturation on attenuation in Massillon sandstone and Vycor porous glass: J. Acoust. Soc. Am., 71, 1458–1468.
- Pipkin, A. C., 1986, Lectures on viscoelasticity theory: Springer Verlag, New York, Inc.
- Samec, P., and Blangy, J. P., 1992, Viscoelastic attenuation, anisotropy, and AVO: Geophysics, 57, 441–450.
- Siringan, F. S., 1993, Coastal lithosome evolution and preservation during an overall rising sea level: East Texas gulf coast and continental shelf: Ph.D. thesis, Rice University.
- Spencer, J. W. Jr., 1981, Stress relaxations at low frequencies in fluid-saturated rocks: Attenuation and modulus dispersion: J. Geophys. Res., 86, 1803–1812.
- Tal-Ezer, H., Carcione, J. M., and Kosloff, D., 1990, An accurate and efficient scheme for wave propagation in a linear viscoelastic medium: Geophysics, 55, 1366–1379.
- White, R. E., 1992, The accuracy of estimating Q from seismic data: Geophysics, 57, 1508–1511.
- Wuenschel, P. C., 1965, Dispersive body waves—An experimental study: Geophysics, 30, 539–551.

APPENDIX A

DERIVATION OF THE 2-D AND 3-D VISCOELASTIC WAVE EQUATION

The constitutive relation for a linear viscoelastic 2-D ($i, j, k = x, y$) or 3-D ($i, j, k = x, y, z$) homogeneous isotropic solid is,

$$\sigma_{ij} = \dot{\Lambda} * \delta_{ij} \epsilon_{kk} + 2\dot{M} * \epsilon_{ij}, \quad (\text{A-1})$$

according to Christensen (1982). It is possible to express the time derivative of ϵ_{ij} as,

$$\dot{\epsilon}_{ij} = \frac{1}{2} (\partial_i v_j + \partial_j v_i). \quad (\text{A-2})$$

Let us define

$$\Pi = \Lambda + 2M \quad (\text{A-3})$$

and use the standard linear solid model for Π and M , i.e.,

$$\Pi = \pi \left(1 - \sum_{\ell=1}^L \left(1 - \frac{\tau_{\epsilon\ell}^p}{\tau_{\sigma\ell}} \right) e^{-t/\tau_{\sigma\ell}} \right) \theta(t) \quad (\text{A-4})$$

and

$$M = \mu \left(1 - \sum_{\ell=1}^L \left(1 - \frac{\tau_{\epsilon\ell}^s}{\tau_{\sigma\ell}} \right) e^{-t/\tau_{\sigma\ell}} \right) \theta(t). \quad (\text{A-5})$$

The definition of Π allows us to define Q independently for P -waves and S -waves through the $\tau_{\epsilon\ell}^p$ (P -waves) and $\tau_{\epsilon\ell}^s$ (S -waves). Using equation (A-1) through (A-3), we find for a diagonal element of $\dot{\sigma}_{ij}$, ($i = j$),

$$\dot{\sigma}_{ij} = (\dot{\Pi} - 2\dot{M}) * \partial_k v_k + 2\dot{M} * \partial_i v_j \quad (\text{A-6})$$

and for an off-diagonal element ($i \neq j$)

$$\dot{\sigma}_{ij} = \dot{M} * (\partial_i v_j + \partial_j v_i). \quad (\text{A-7})$$

By evaluating parts of the convolution and defining the memory variables $r_{ij\ell}$, we can write equation (A-6) as

$$\begin{aligned}
\dot{\sigma}_{ij} = & \left(\pi \left(1 - \sum_{\ell=1}^L \left(1 - \frac{\tau_{\epsilon\ell}^p}{\tau_{\sigma\ell}} \right) \right) \right. \\
& - 2\mu \left(1 - \sum_{\ell=1}^L \left(1 - \frac{\tau_{\epsilon\ell}^s}{\tau_{\sigma\ell}} \right) \right) \left. \right) \partial_k v_k \\
& + 2\mu \left(1 - \sum_{\ell=1}^L \left(1 - \frac{\tau_{\epsilon\ell}^s}{\tau_{\sigma\ell}} \right) \right) \partial_i v_j + \sum_{\ell=1}^L r_{ij\ell}
\end{aligned} \quad (\text{A-8})$$

and equation (A-7) as

$$\dot{\sigma}_{ij} = \mu \left(1 - \sum_{\ell=1}^L \left(1 - \frac{\tau_{\epsilon\ell}^s}{\tau_{\sigma\ell}} \right) \right) (\partial_i v_j + \partial_j v_i) + \sum_{\ell=1}^L r_{ij\ell}. \quad (\text{A-9})$$

Applying the same technique as was used to derive equation (11) from equation (9) yields for diagonal $r_{ij\ell}$ ($i = j$)

$$\begin{aligned}
\dot{r}_{ij\ell} = & -\frac{1}{\tau_{\sigma\ell}} \left(r_{ij\ell} + \left(\pi \left(\frac{\tau_{\epsilon\ell}^p}{\tau_{\sigma\ell}} \right) - 2\mu \left(\frac{\tau_{\epsilon\ell}^s}{\tau_{\sigma\ell}} \right) \right) \partial_k v_k \right. \\
& \left. + 2\mu \left(\frac{\tau_{\epsilon\ell}^s}{\tau_{\sigma\ell}} \right) \partial_i v_j \right) \quad 1 \leq \ell \leq L
\end{aligned} \quad (\text{A-10})$$

and off-diagonal ($i \neq j$)

$$\dot{r}_{ij\ell} = -\frac{1}{\tau_{\sigma\ell}} \left(r_{ij\ell} + \mu \left(\frac{\tau_{\epsilon\ell}^s}{\tau_{\sigma\ell}} \right) (\partial_i v_j + \partial_j v_i) \right) \quad 1 \leq \ell \leq L. \quad (\text{A-11})$$

Adding Newton's second law,

$$v_i = \frac{1}{\rho} \partial_j \sigma_{ij}, \quad (\text{A-12})$$

yields the viscoelastic wave equation. Specializing to two dimensions ($i, j, k = x, y$) and one standard linear solid ($L = 1$) results in equation (17).